

# Spatially and spectrally resolved quantum path interference with chirped driving pulses

Stefanos Carlström<sup>1,6,\*</sup>, Jana Preclíková<sup>1,2,6</sup>, Eleonora Lorek<sup>1</sup>,  
Esben Witting Larsen<sup>1</sup>, Christoph M Heyl<sup>1</sup>, David Paleček<sup>3,4</sup>,  
Donatas Zigmantas<sup>3</sup>, Kenneth J Schafer<sup>5</sup>, Mette B Gaarde<sup>5</sup>,  
and Johan Mauritsson<sup>1,†</sup>

<sup>1</sup>Department of Physics, Lund University, Box 118, 222 10 Lund, Sweden

<sup>2</sup>Department of Physics and Technology, University of Bergen, 5007 Bergen, Norway

<sup>3</sup>Department of Chemical Physics, Lund University, Box 124, 222 10 Lund, Sweden

<sup>4</sup>Department of Chemical Physics, Charles University in Prague, Ke Karlovu 3,  
121 16 Praha 2, Czech Republic.

<sup>5</sup>Louisiana State University, Baton Rouge, 70803-4001, Louisiana, United States of America.

<sup>6</sup>These authors contributed equally to this work.

E-mail: \*stefanos.carlstrom@fysik.lth.se, †johan.mauritsson@fysik.lth.se

**Abstract.** We measure spectrally and spatially resolved high-order harmonics generated in argon using chirped multi-cycle laser pulses. Using a stable, high-repetition rate laser we observe detailed interference structures in the far-field. The structures are of two kinds; off-axis interference from the long trajectory only and on-axis interference including the short and long trajectories. The former is readily visible in the far-field spectrum, modulating both the spectral and spatial profile. To access the latter, we vary the chirp of the fundamental, imparting different phases on the different trajectories, thereby changing their relative phase. Using this method together with an analytical model, we are able to explain the on-axis behaviour and access the dipole phase parameters for the short ( $\alpha_s$ ) and long ( $\alpha_l$ ) trajectories. The extracted results compare very well with phase parameters calculated by solving the time-dependent Schrödinger equation. Going beyond the analytical model, we are also able to successfully reproduce the off-axis interference structure.

PACS numbers: 42.65.Ky, 42.65.Re

*Keywords:* Quantum path interference, high-order harmonic generation, dipole phase parameters

Submitted to: *New J. Phys.*

## 1. Introduction

High-order harmonic generation (HHG) is a nonlinear optical process, in which a comb consisting of multiples of the driving laser frequency  $\omega_0$  is emitted coherently after interaction with a target [1, 2]. HHG and the understanding of the process itself has led to the field of attosecond physics [3], which enables the time-resolved observation of electron dynamics [4, 5, 6, 7].

The HHG process can be understood using a semi-classical three step model in which an electron is first ionized by tunnelling, is subsequently accelerated in the laser field, and finally returns to the ion core and upon recombination releases its excess kinetic energy leading to the emission of high energy photons [8, 9]. The generated harmonics are of odd orders since the process is repeated every half cycle of the laser field. This semi-classical understanding has been verified extensively through comparison with experiments and with more sophisticated calculations based on the integration of the time-dependent Schrödinger equation (TDSE) within the single-active-electron (SAE) approximation, either in its full numerical form [10] or within the strong field approximation (SFA) [11]. From this three-step model for HHG, it follows that for each harmonic energy there are multiple quantum paths (QPs) the electron can follow in the continuum. They correspond to different pairs of ionization and return times ( $t_i, t_r$ ), that give rise to the same kinetic energy upon return. The two first QPs, termed the short and long QPs, both return within one cycle after ionization, with the short QP being released later and returning earlier than the long QP. The emission generated from each of these two QP contributions has different macroscopic coherence properties [12, 13, 14] because of the different microscopic phase that is imparted via the semi-classical action accumulated along each path. As we will describe in more detail below, this phase is approximately proportional to the cycle-averaged laser intensity with a phase coefficient  $\alpha$  that increases with the time spent in the continuum. This means that the intensity dependence of the short-path contribution to the harmonic emission is much smaller than that of the long-path contribution. Therefore, the short QP emission has a smaller spectral and spatial divergence imparted by the temporal and radial variation of the laser intensity in the generation region.

The dipole properties of the HHG process may lead to various interference effects, since the same final energy is generated from several different trajectories. Interferences appearing as spectral and/or spatial structures in the harmonic far-field emission have been reported and identified as interferences between the short and the long quantum path contribution, known as quantum path interferences (QPI) [15, 16, 17, 18, 19]. Other works identify interferences arising within the long path contribution only due to spatio-temporal phase and amplitude modulations in the generation medium [20, 21] or due to the spectral interference of adjacent harmonics [22]. The emission from the short QP contribution has been characterized in much more detail [23, 24, 25] than that from the long QP contribution [22] as the latter is more difficult to accurately phase match and control experimentally [15, 19].

In this paper we present a detailed experimental characterization of the phase properties of the short and long QP contributions to HHG, via QPI in both the spectral and spatial domain which we control through the chirp of the generating laser pulse, also changing the pulse duration and the intensity. We identify and distinguish quantum path interferences from macroscopic interference effects arising within the emission of the long trajectory. We use a commercial turn-key laser system that produces long multi-cycle pulses (with durations  $\geq 170$  fs, corresponding to  $\geq 50$  cycles at the driving wavelength  $\lambda = 1030$  nm), which yield spatially and spectrally well-resolved harmonics with high signal-to-noise ratio. The stable operation of the laser in combination with the long and controllable pulses allow us to observe and characterize the QPI for a range of harmonics in argon spanning from harmonic 11, which is below the ionization threshold, to harmonic 37. In a single spectrum, clear spatial and spectral modulation of the harmonic order is visible, predominantly for the contribution of larger spatial and spectral divergence, i.e. the long QP contribution. The interference between the short and the long QPs, however, is not visible from one spectrum alone, but it is sensitive to intensity variation of the driving field. Therefore, controlling the shape of the driving pulse by adding a frequency chirp, the HHG process is affected through the increase in pulse duration and a decrease of the peak intensity. This reveals the interference between the short and long QPs, since their respective phases depend differently on the peak intensity. Additionally, the sign of the driving pulse chirp changes the spectral phase of the harmonic emission and in particular influences the QPs differently.

We implement a model based on the semi-classical description of HHG [14] as driven by a laser pulse, which is Gaussian in the temporal and spatial domain. This simple model captures the observed on-axis short–long QPI features very well and can be used to extract the phase coefficients  $\alpha_s$  and  $\alpha_l$  from the experimental results. We also compare the experimental results to numerical calculations performed both within the SAE-TDSE and the SFA. We measure experimental values for  $\alpha_l$  in good agreement with those obtained in [15, 26]. For  $\alpha_s$  we measure values that are small and negative for a range of low-order harmonics, indicating that the interaction between the returning electron and the ionic potential plays a substantial role in the generation of these harmonics. Negative values for  $\alpha_s$  have been predicted in some calculations [24, 25] but have not to our knowledge been observed experimentally to this date.

We further investigate the off-axis interference structures by employing a more complete, but numerical model. The spectral–spatial modulation due to the long QP is very well reproduced by this model and explains the significance of the contributions that go beyond the analytical model, namely phase curvature effects of higher order than parabolic and the intensity dependence of the dipole phase parameters  $\alpha_{s/l}$ .

The paper is organized as follows: in section 2, the experimental method used to obtain the data is briefly outlined, and in section 3, these data are presented. In section 4, the mathematical model is described and in section 5 the quantum mechanical calculations used to verify our modelling are presented. Whereas sections 4–5 are mainly concerned with the short–long QPI, section 6 describes the interference structures visible

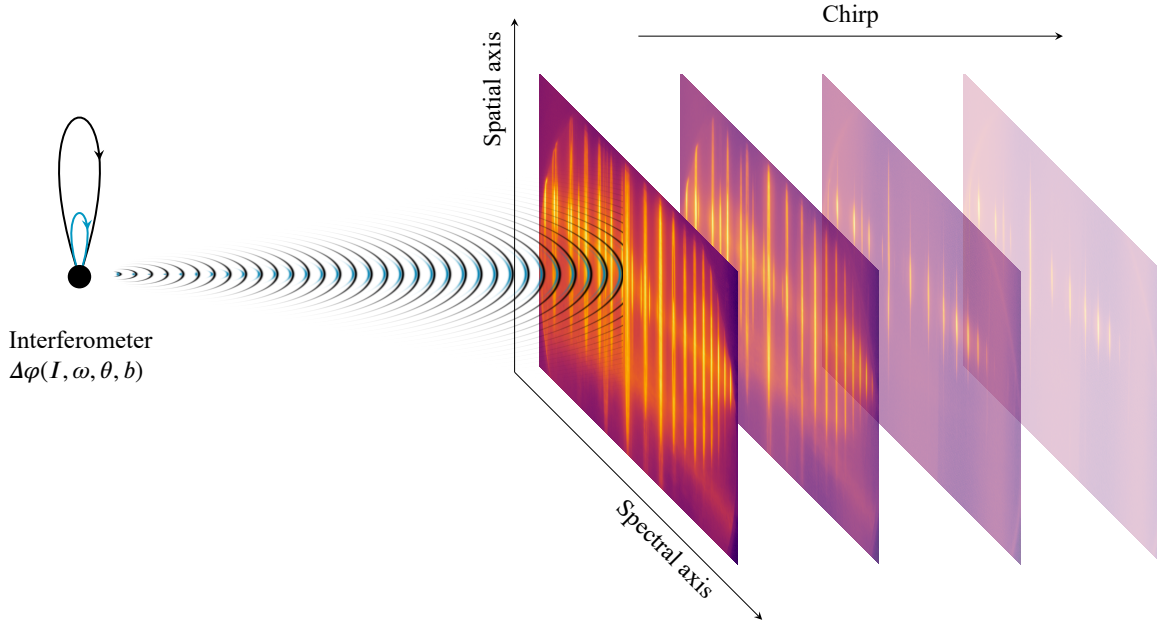


**Figure 1.** Experimental scheme; in our experiment the HH emission consists of contributions related to the two shortest QPs: short (blue) and long (black). We gradually vary the chirp of the driving pulses and observe spatially and spectrally resolved HH. The experiment can be understood as an interferometer, where the phase difference  $\Delta\varphi$  between the long and short trajectories varies with the driving intensity  $I$ , the emitted frequency  $\omega$  and the angle of emission  $\theta$  and the chirp parameter  $b$ .

off-axis, where no short QP is present. Finally, in section 7 we discuss our results and what we can extract from them.

## 2. Experimental method

The high-order harmonics (HHs) were generated in argon by a commercially available compact Yb:KGW PHAROS laser (Light Conversion). The pulse energy was 150  $\mu\text{J}$ , the central wavelength  $\lambda = 1030\text{ nm}$  and the repetition rate was set to 20 kHz. The pulse-to-pulse stability of this laser is  $< 0.5\%$  rms over 24 hours. The duration and chirp of the pulses were varied by adjusting the grating compressor. The adjustment of the grating enabled a gradual change of the pulse duration from negatively chirped pulses of 500 fs to Fourier-transform (FT) limited pulses of  $\tau_{\text{FT}} = 170\text{ fs}$  to positively chirped pulses of 500 fs (corresponding to 50–145 cycles) in 106 steps. The acquisition time for one image was around 80 ms, averaging around 1600 shots.

The calibration of the pulse duration as a function of the grating position was based on the peak intensity of the pulse. The observed cut-offs of HHs 25–37 were mapped to a specific driving intensity using the cut-off law

$$q\hbar\omega_0 = 3.17 \frac{e^2 I_0(\tau)}{2c\epsilon_0 m \omega_0^2} + I_p = 3.17 U_p + I_p, \quad (1)$$

where  $q$  is the harmonic order,  $\hbar$  is the reduced Planck constant,  $\omega_0$  is the angular central frequency of the driving laser,  $I_p$  is the ionization potential of argon,  $e$  and  $m$  are the charge and the mass of electron,  $\epsilon_0$  is the permittivity of vacuum and  $I_0(\tau)$  is the peak laser intensity for the pulse of duration  $\tau$ , at the centre of the driving field. The laser peak intensity is taken to vary as

$$I_0(\tau) = I_0(\tau_{\text{FT}}) \frac{\tau_{\text{FT}}}{\tau}, \quad (2)$$

where the peak intensity at FT-limited duration  $I_0(\tau_{\text{FT}})$  is on the order of  $10^{14} \text{ W cm}^{-2}$ . The laser beam with a diameter of 3.5 mm was focused by an achromatic lens with a focal length 100 mm, resulting in a beam waist of  $18 \mu\text{m}$  (estimated using Gaussian optics). As generating medium argon gas was used, supplied through an open-ended, movable gas nozzle with  $90 \mu\text{m}$  inner diameter. The relative position of the nozzle and the laser focus was such that phase matching allowed the observation of both short and long trajectory harmonics [27, 28].

The generated harmonic emission was analysed by a flat-field grazing-incidence XUV spectrometer (based on Hitachi Grating 001-0639, with the nominal line-spacing of 600 lines/mm). The grating diffracted and focused the harmonics in the dispersive plane and reflected them in the perpendicular direction onto a 78 mm diameter microchannel plate (MCP, Photonis), which was imaged by a CCD camera (Allied Vision Technologies, Pike F-505B with a pixel size of  $3.45 \mu\text{m} \times 3.45 \mu\text{m}$ ; the resolution was set to 2000 pixels  $\times$  2000 pixels and the dynamic range to 14 bits). This arrangement allowed to study the spectral content of the emission as well as the divergence of the individual harmonics. The HH spectra were recorded for 106 positions of the pulse compressor grating, see figure 1. A more detailed description of the setup can be found in [29].

### 3. Experimental results

A typical image of HHs on an MCP is displayed in figure 2(a) for the case of a FT-limited driving pulse. The HHs are both spatially and spectrally divergent, with clear ring structures appearing around a strong, narrow central structure. The off-axis structures are attributed to the long QP only, whereas the on-axis structures contain both QPs. However, the on-axis structures do not show to any visible modulation in a single spectrum. To reveal the on-axis interference, the acquired HH spatial-spectral profiles for 106 different values of the chirp parameter were analysed by plotting different lineouts of the images as a function of the driving pulse duration. The spatial-spectral profile of  $q = 17$  is shown magnified in figure 2(b). The horizontal axis (and lineouts) correspond to the spectral variation, whereas the vertical axis (and lineouts) to the spatial variation. The lines represent regions of interest, from which subfigures (c)–(f) are extracted. (d) and (e) are the spectral and spatial lineouts of the central area of the generated harmonics with contribution from both the long and short trajectories, while the off-axis lineouts (c) and (f) show mainly behaviour of the long trajectory

contribution, therefore lacking interference between the two trajectories (however, long–long interference remains). In the following analysis we focus on the on-axis areas, where short–long QPI patterns are apparent, as in (d) and (e). The spatial and spectral lineouts for other orders are presented in sections 4.1 and 4.2. We return to the off-axis interference structures in section 6.

#### 4. Mathematical model

To explain and analyse the observed QPI, we have developed a mathematical model based on the interplay of the HH contributions from different QPs; similar to the simple model of [14]. We concentrate on the two first trajectories, the so called short ( $s$ ) and long ( $l$ ). The main difference is that, since the long trajectory spends more time in the continuum, it acquires more phase which leads to larger divergence, both spatially and spectrally. This phase is labelled  $\Phi_{s/l}$ . Using the SFA, the dipole phase can be calculated by integrating the semi-classical action [11, 25] (in atomic units):

$$\Phi_{s/l}(t_i, t_r, \mathbf{p}) = q\omega_0 t_r - \int_{t_i}^{t_r} dt \left\{ \frac{[\mathbf{p} + \mathbf{A}(t)]^2}{2} + I_p \right\}, \quad (3)$$

where the trajectory of the electron is defined by its ionization time,  $t_i$ , return time,  $t_r$ , and momentum  $\mathbf{p}$ .  $\mathbf{A}(t)$  is the vector potential of the driving field. In figure 3, (3) is plotted for a few different harmonic orders, using the experimental conditions of the present work. The ionization time  $t_i$  and the return time  $t_r$  are found by solving Newton's equations of an electron in an electric field. The general behaviour of the phases as a function of intensity leads us to the following approximate expression:

$$\Phi_{s/l}(r, z, t) = \Phi_{s/l}^0 + \alpha_{s/l} I(r, z, t), \quad (4)$$

where  $\Phi_{s/l}^0$  is a phase offset and  $\alpha_{s/l}$  are slopes of the phases as function of the intensity [14]. This adiabatic model is valid for the experimental conditions of the present work [30].

In our simple model, we assume a tight-focus geometry with a small interaction volume and we only consider HH generated in the focal plane  $z = 0$ .

##### 4.1. Divergence

To model the behaviour of the harmonics along the divergence axis as the pulse duration varies, the emission from the two trajectories is approximated as a sum of Gaussian beams. Such beams can be propagated to the far field analytically (in the paraxial approximation), and the geometrical properties necessary are determined from the experimental conditions. In Appendix A.1, the full derivation of the divergence model can be found. The main result is that the total far field can be written in cylindrical coordinates as

$$E_{\text{detector}}(r, z) = E_s(r, z) + E_l(r, z), \quad (5)$$

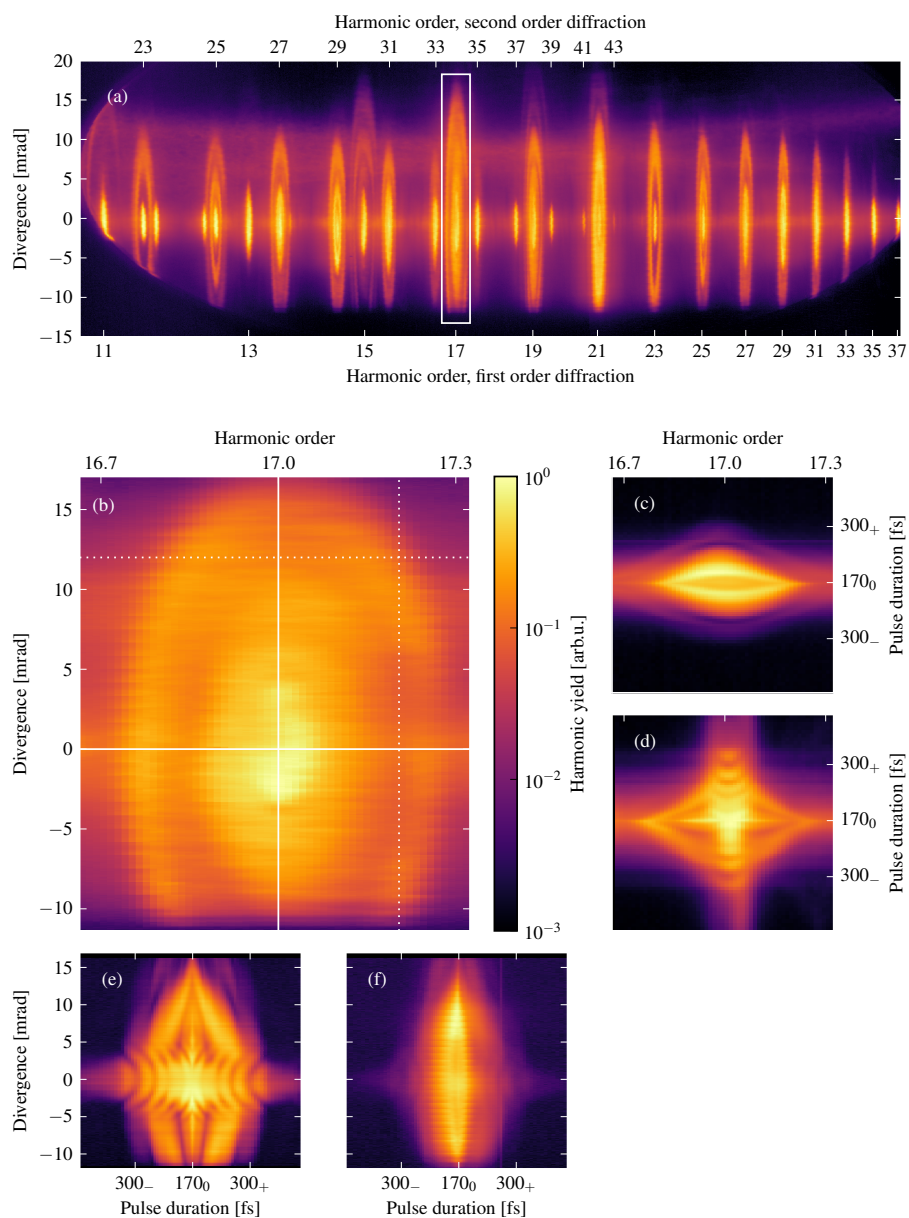


**Figure 2.** (a) Observed HHs as recorded by MCP under driving with transform-limited pulses, numbers indicate the spectral position of the first and second order diffraction of HHs for  $q = 11 - 43$ , the rectangle shows the area, for which an example of the analysis is given. (b) Magnified image of the area around HH17. The solid lines indicate where the lineouts on-axis and on the central harmonic energy, respectively, were made. Similarly, the dotted lines indicate where the lineouts off-axis and off the central harmonic energy were made. (c) shows the off-axis spectral lineouts corresponding mainly to the long trajectory contribution, while (d) shows the on-axis spectral lineout with a clear QPI pattern. Similarly, (e) shows the on-centre spatial lineout with a clear QPI pattern and (f) is a spatial lineout covering mainly the long trajectory contribution. 300<sub>+/-</sub> fs means 300 fs pulse duration with positive/negative chirp; 170<sub>0</sub> fs means FT-limited duration. The colour scale is logarithmic and is the same in all figures throughout the article, unless stated otherwise.

where

$$E_{s/l}(r, z) = C_{s/l} I_0^{\frac{n}{2}}(\tau) W(z) \exp[-iG(r, z; r_0, z^R) + i\Phi_{s/l}(r, z)]. \quad (6)$$

$C_{s/l}$  are weights for the trajectories,  $n$  is a nonlinearity parameter,  $W(z)$  and  $G(r, z; r_0, z^R)$  are functions depending on the geometry as well as the ionization process, whereas  $\Phi_{s/l}$  is the phase in (4), which only depends on the atomic properties.  $r_0$  is the beam waist (18  $\mu\text{m}$ ) and  $z^R$  the effective Rayleigh range ( $\sim 1$  mm).

The spatial profiles of the generated HH beams are calculated for  $q = 11 - 37$ , using the variation of the pulse duration  $\tau$  as in the experiment. The experimental input values are  $\lambda$ ,  $r_0$ ,  $z$  and  $I_0(\tau)$  [determined using (1)], whereas unknown parameters are  $\Phi_s^0, \Phi_l^0, \alpha_s, \alpha_l, n$  and the ratio  $C_l^2 : C_s^2$ . In our procedure we neglect the influence of phase offset difference  $|\Phi_s^0 - \Phi_l^0|$  – it influences only the phase of the fringe pattern (with  $2\pi$  periodicity), but not the shape. The procedure for retrieving the values of  $\alpha_{s/l}$  for the different harmonics is the following: 1) The experimental spatial lineouts are normalized separately for each harmonic, 2) positions of interference maxima and minima are determined [shown as the white and black lines overlaid in figure 4] in order to highlight the shape of the interference pattern, 3) the parameters of the model are then fitted such that the frequency of the fringes and their curvature in the model match that of the experiment (see figure 4 for  $q = 17$ ). The phase difference  $(\alpha_l - \alpha_s)I$  between

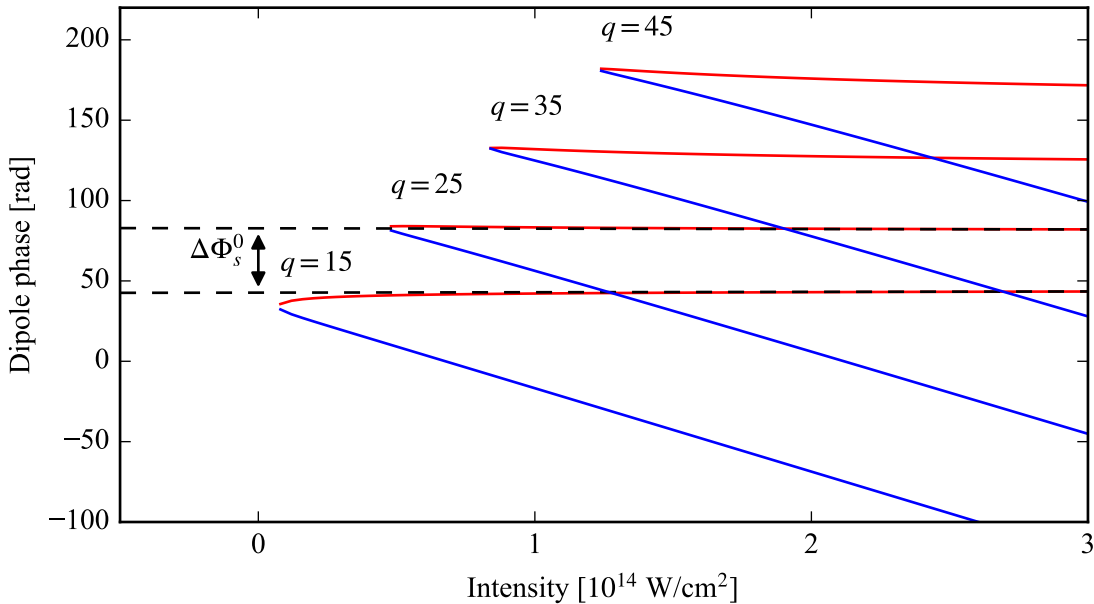


**Figure 3.** Dipole phase as a function of intensity, for different high-order harmonics of  $\lambda = 1030$  nm, calculated using (3). The red (blue) lines correspond to the short (long) trajectories. For the intensities used in the experiment ( $4 \times 10^{13}$   $\text{W cm}^{-2}$  to  $1 \times 10^{14}$   $\text{W cm}^{-2}$ ), the curves are well approximated by (4). The two dashed lines are fits to the asymptotes of the red lines, i.e. they are not perfectly horizontal. The slopes of these fits are  $-\alpha_s$ .



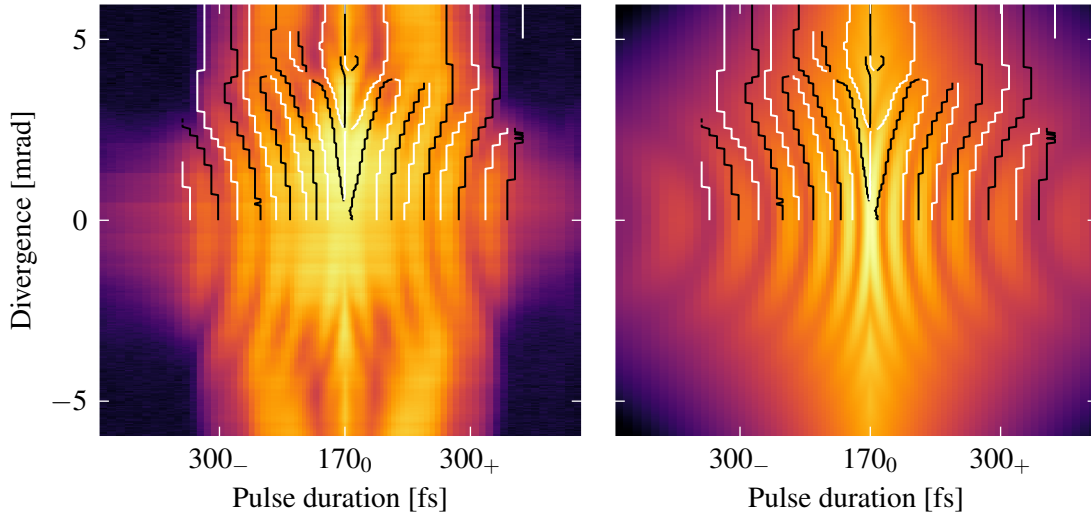


**Figure 4.** Illustration of the fitting procedure for retrieval of the values of  $\alpha_{s/l}$  for the different harmonics. In the left panel the experimental data are shown with the maxima (white lines) and minima (black lines) extracted. In the right panel, the coloured map is the result of the mathematical model described in section 4.1, while the lines are the same as in the left panel.  $300_{+/-}$  fs means 300 fs pulse duration with positive/negative chirp;  $170_0$  fs means FT-limited duration.

the two trajectories can by itself explain the observed frequency of the fringes, on-axis. However, we have more information available in that the fringe pattern has a curvature, which allows us to retrieve not only the difference between  $\alpha_{l/s}$ , but also their absolute values. This is because the curvature of the fringes depends on mean value  $(\alpha_l + \alpha_s)/2$  as well as on the difference  $\alpha_l - \alpha_s$ , which is why an iterative fit has to be made. The contrast and the overall intensity of the divergence pattern, are mainly affected by nonlinearity parameter  $n$  and by the ratio of long and short trajectory contribution  $C_l^2 : C_s^2$ .

For  $q = 15 - 21$ , automated fitting of the model to the experimental data could be done, while for the higher harmonics, a visual fit was the only option, since the interference signal was too weak for these harmonics. The retrieved values of the parameters are listed in table 1.

In figure 5(b), the far-field divergence profiles as simulated by the spatial model are shown for the values of  $\alpha_{s/l}$  as extracted by the fitting procedure described above (these values are presented in table 1). To be noted is that the model manages to reproduce the hyperbolic fringes visible for divergences smaller than  $\sim 5$  mrad; however, the prominent ring structure visible for larger divergences are not reproduced by this model. As will be discussed in more detail in section 6, the rings arise when including higher-order terms than parabolic in the phase curvature. The ring structure in a given harmonic depend on higher-order corrections to the harmonic phase beyond the simple linear dependence on the intensity with phase coefficient  $\alpha$ . In particular, the far-field radiation pattern

for the long-trajectory harmonics consists of interfering contributions from parts of the near-field where these harmonics belong to the plateau and parts of the near-field where these harmonics belong to the cut-off. Such contributions to the same harmonic will have different values of  $\alpha$ .

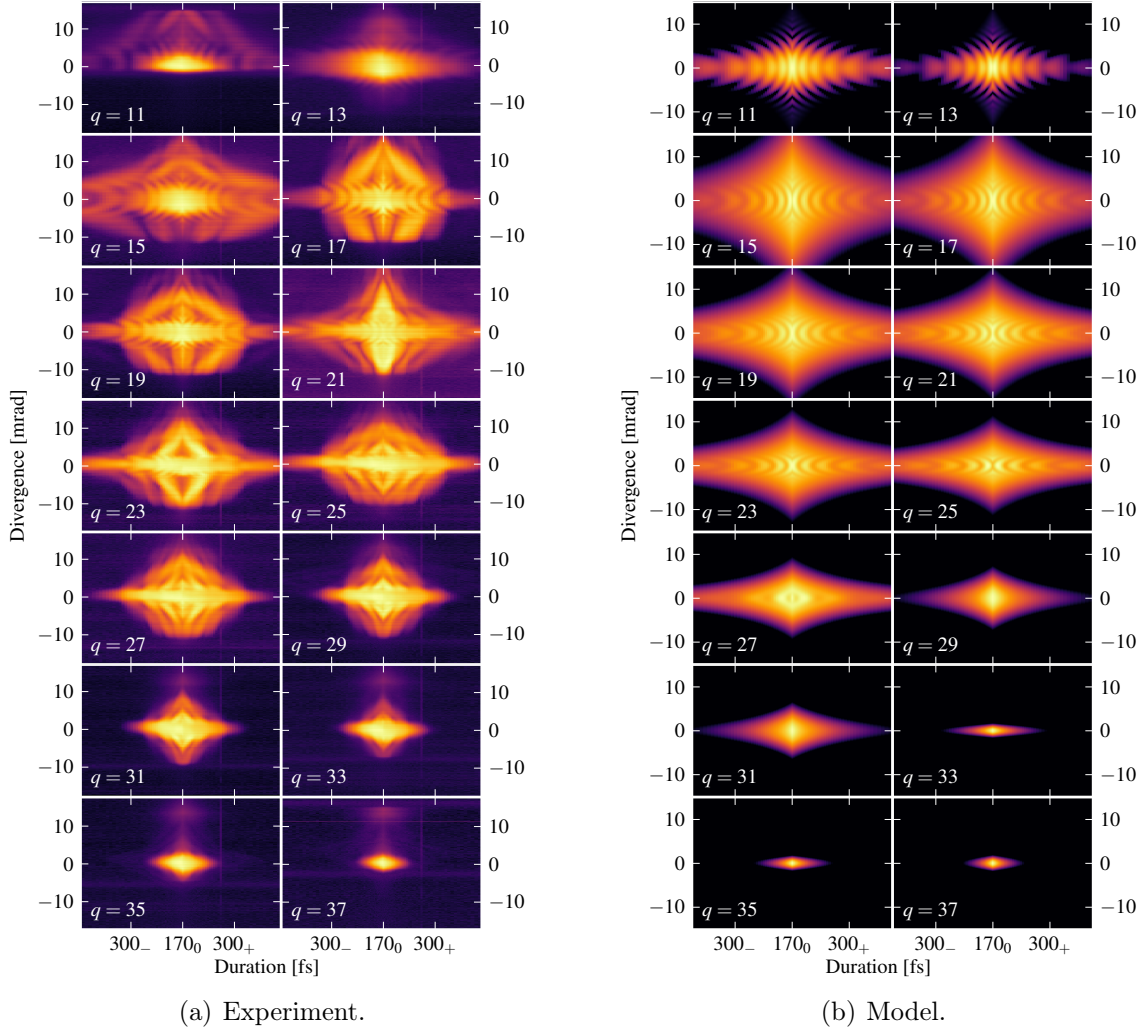


**Figure 5.** Comparison of experimental and modelled data for variation of divergence profiles with gradually varied duration of the driving pulses for  $q = 11 - 37$ . In the left part of the images the driving pulses are negatively chirped, whereas in the right part are positively chirped. The signal for the low harmonic orders, especially apparent for  $q = 11$ , is limited to positive divergence by the shape of the MCP.

**Table 1.** Values of parameters used in the divergence model [see figure 5(b)] for the simulation of the spatial profiles of generated HH.

$q$	11	13	15	17	19	21	23	25	27	29	31	33	35	37
$\alpha_s / (10^{-14} \text{ cm}^2 \text{ W}^{-1})$	-10	-11	-10	-10	-10	-9	-7	-5	5	15	15	18	20	24
$\alpha_i / (10^{-14} \text{ cm}^2 \text{ W}^{-1})$	50	50	51	50	43	43	40	38	35	35	33	31	28	24
$n$	6	8	7	7	6	6	6	6	7	10	10	11	14	17
$C_l^2 : C_s^2$	2	2	100	100	100	100	100	100	100	100	100	30	50	5

#### 4.2. Spectrum

To understand the variation of the spectral profile as a function of the driving field chirp, it is important to model the temporal behaviour of the harmonic generation, and particularly its response to change in instantaneous frequency. The detailed derivation can be found in [Appendix A.2](#). The main result this time is that the field contribution for a given harmonic from the short/long trajectory can be written

$$E_{s/l}(t) = C_{s/l} I^{\frac{n}{2}}(t) \exp \left[ i q \omega_0 + i \frac{q b(\tau)}{2} t^2 + i \alpha_{s/l} I(t) + i \Phi_{s/l}^0 \right]. \quad (7)$$

The far-field spectra of the generated HHs are computed as the Fourier transform of the sum of the fields generated by the short and long trajectory contributions

$$S(\omega) = \mathcal{F}[E_s(t) + E_l(t)], \quad (8)$$

and the intensity in the far field is given by

$$I(\omega) \propto |S(\omega)|^2. \quad (9)$$

The simulated spectra are shown in [figure 6\(b\)](#). The experimental input parameters are the same as for the spatial profile simulation and the retrieved values of the parameters are listed in [table 2](#). Again,  $\Phi_{s/l}^0$  is assumed to be zero, since it only influences the phase of the interference fringes, but not their shape. When determining the values of  $\alpha_{s/l}$ , the main attention is given to the width of the measured spectra and to the curvature of the QPI fringes. The values were found by a pure visual fit of the model to the experimental data, no automated fitting was employed. The  $n$  was kept same as in the simulation of the divergence lineouts, while the ratio  $C_l^2 : C_s^2$  had to be decreased, due to the fact that only the middle part of the divergence cone is evaluated [see [figure 2\(d\)](#)]. In this cone, the relative contribution of the short trajectory is much stronger than when a broad divergence region is considered, leading to a lower ratio  $C_l^2 : C_s^2$ .

The asymmetric behaviour of the central part of the spectra with respect to the chirp parameter (clearly apparent in [figure 6\(a\)](#) for  $q = 13, 15, 17$ ), enables us to determine negative values of  $\alpha_s$  in the region below threshold and in the plateau. It is possible to make this identification, since the central part of the spectrum is dominated by the short trajectory contribution. The instantaneous frequency of the generated HH field is described by [\(A.15\)](#) – the time derivative of the argument of [\(7\)](#). For negatively chirped pulses, the chirp of the driving pulse [the second term in [\(A.15\)](#)] has the same sign as the chirp introduced by the dipole phase [third term in [\(A.15\)](#)] and a broad spectrum of frequencies is generated. In contrast, when the pulse is positively chirped, the second and third terms have opposite signs and partly compensate each other, with a narrower spectrum as the result. The negative sign of  $\alpha_s$  for the low orders leads to this compensation occurring for negatively chirped pulses (the left side of the spectra in [figure 6](#)), while for higher orders, the compensation occurs for positively chirped pulses

(the right side of the spectra in figure 6). The sign change occurs around harmonic 23, where the narrowest spectrum of short trajectory is found for FT-limited pulses. For the long trajectory, all  $\alpha_l$  are positive, such that the compensation always occurs for positively chirped pulses.

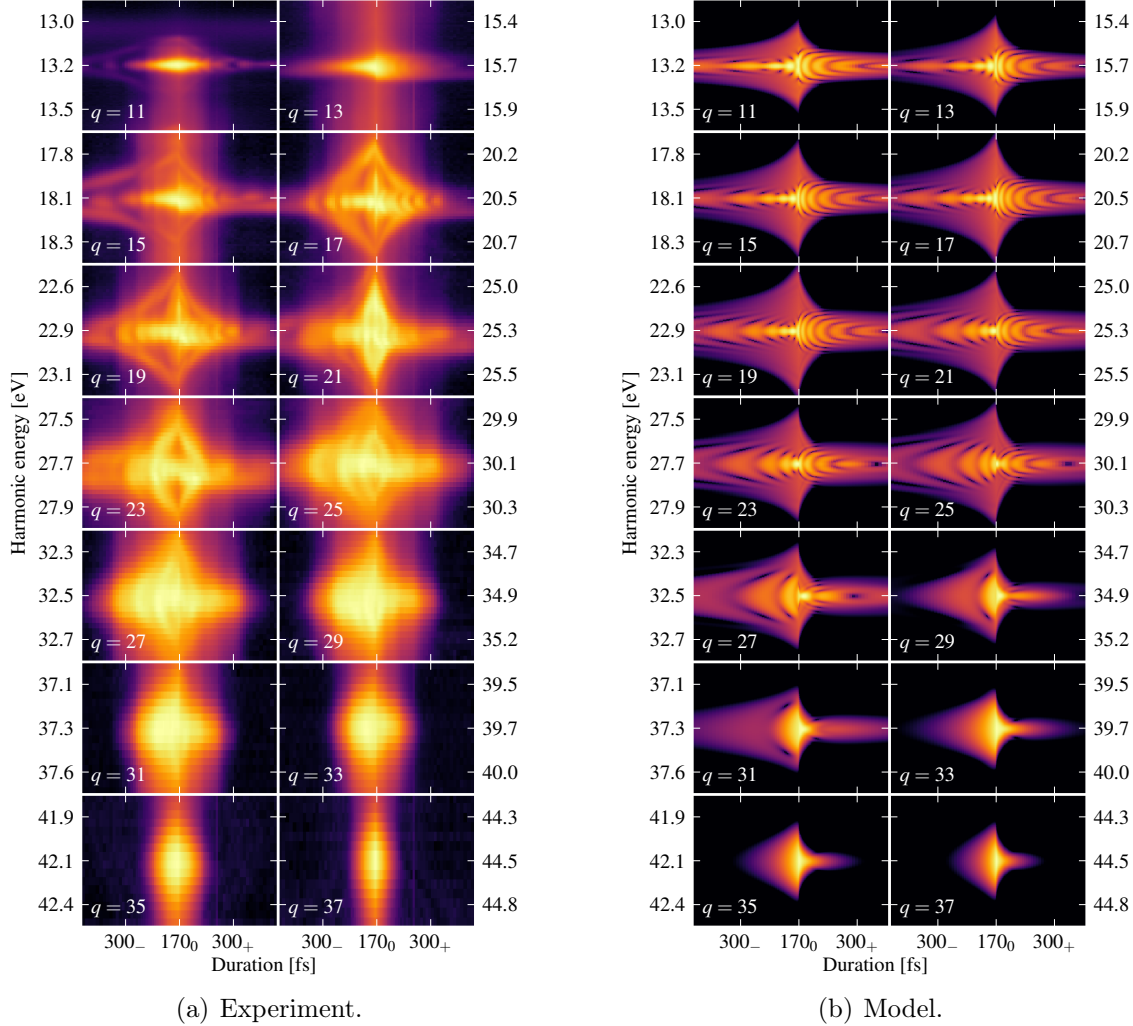


**Figure 6.** Comparison of experimental and modelled data for variation of HH spectra with gradually varied duration of the driving pulses for  $q = 11 - 37$ . In the left part of the images the driving pulses are negatively chirped, whereas in the right part they are positively chirped. As is explained section 4.2, the fit of the spectral model to the data was purely visual, matching the the amount of fringes and their positions.

### 4.3. Dipole phase parameters

In figure 7, the retrieved values of  $\alpha_{s/l}$  from both the divergence model and the spectral model, are shown. The values of  $\alpha_{s/l}$  predicted by different theoretical calculations and retrieved for various experimental conditions (driving wavelengths  $\lambda$  and intensities  $I$ ) can be compared, by expressing them in dimensionless values  $\alpha_{s/l}^*$  related to the optical



which could explain the larger variation in the data. An estimate of the error is given by the mean discrepancy between the two models, which is  $\sim 2.5 \times 10^{-14} \text{ cm}^2 \text{ W}^{-1}$  for the short trajectory and  $\sim 6 \times 10^{-14} \text{ cm}^2 \text{ W}^{-1}$  for the long trajectory.

## 5. Quantum mechanical calculations

For comparison, calculations of the HH yield are performed by integrating the TDSE for a range of intensities using a newly developed graphics processing unit (GPU) implementation of the algorithm outlined in [33]. For a large range of intensities, the time-dependent dipole acceleration  $a(t, I)$  of the atom is computed, and the quantum path distributions (QPDs) are extracted in the same manner as described in great detail in [34]; first a Fourier transform is performed to get the spectrum  $a(\omega, I)$  and subsequently, for each harmonic order  $q$ , a Gabor transform is performed along the intensity axis to obtain the QPDs  $a(q; I, \alpha)$ . In figure 8, the QPDs leading to emission of the different harmonics are plotted in an intensity range around the experimental intensity, along with the experimentally retrieved values of  $\alpha_{s/l}$  as presented in tables 1, 2. For comparison, the same procedure is performed for the SFA; the main difference is that the long trajectory is much more pronounced in the SFA, whilst the TDSE also shows longer trajectories. In general, though, they both agree well with the experimental results.

One important difference compared to the models presented above, is that these calculations are performed at slightly lower intensity,  $7 \times 10^{13} \text{ W cm}^{-2}$  as compared to  $1 \times 10^{14} \text{ W cm}^{-2}$ . These calculations are performed using a trapezoidal pulse shape, with exactly this intensity, while in the experiment and the models, the pulse shape is Gaussian, which naturally spans a distribution of intensities, up to the nominal intensity,  $I_0(\tau_{\text{FT}})$ .

## 6. Analysis of off-axis ring-like structures

In figure 9, a theoretical far-field spectrum calculated for the parameters of the experiment is shown. The time-dependent dipole acceleration  $a(t)$  is calculated by the TDSE for a set of atoms in the focal plane. The collective emission is propagated to the far-field, as is described below in section 6.2. Qualitatively, the agreement with the experimental spectrum in figure 2(a) is very good; the appearance of further spatial modulation can be attributed to the lack of intensity averaging as is present in the experiment. Notably, the ring-like structures off-axis (i.e. for divergences  $\geq 5 \text{ mrad}$ ) are present, whereas they are missing in the results of the Gaussian model in its parabolic phase approximation as presented in figure 5(b). This can be understood as follows: The harmonic emission can be written as

$$E(r, t) = A(r, t) \exp[i\Phi(r, t)], \quad (11)$$

where  $A(r, t)$  is the amplitude and  $\Phi(r, t)$  the phase, both dependent on the location and time of emission. If we assume we can divide the emission into different contributions

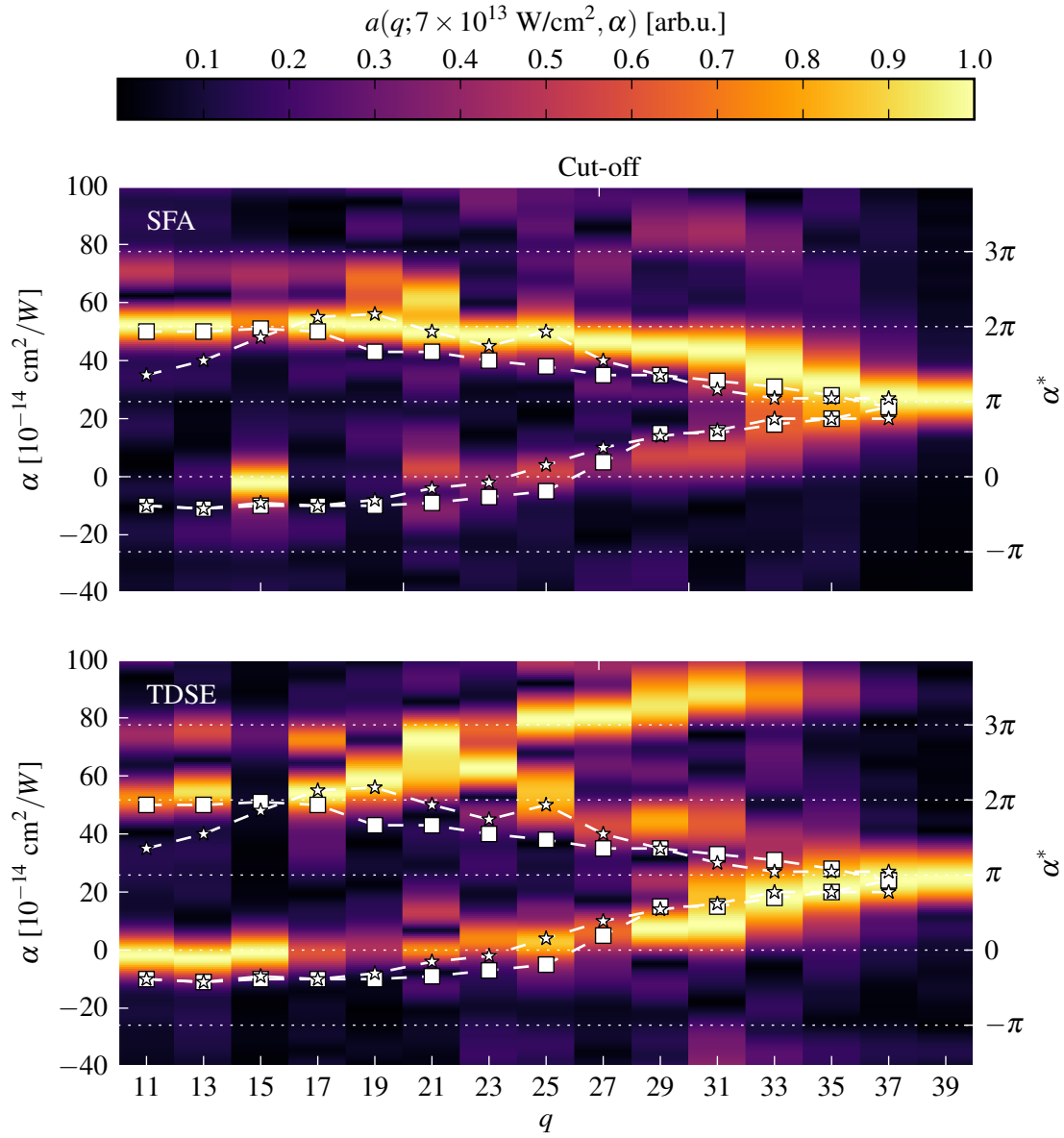


**Figure 8.** Quantum path distributions (QPDs), normalized, for the harmonics  $q = 11$ – $39$ , calculated at the driving field intensity  $7 \times 10^{13} \text{ W cm}^{-2}$ . Bright regions correspond to more likely values of  $\alpha$  for a certain harmonic order. The white lines correspond to the experimentally retrieved values of  $\alpha$ , with the lower values belonging the short trajectories and the higher values to the long trajectory. The right-hand  $\alpha^*$  (the variable conjugate to  $I$ ) scale is given in radians in accordance with (10).

In the SFA, the long trajectory is significantly more prevalent compared to the short trajectory, and this has been observed before [34]. In contrast, the TDSE yields short and long trajectories of comparable weight, and even longer trajectories are visible; also this is a previously known result [35]. The third trajectory has not been observed in the experiments, which might be due to the unfavourable phase matching conditions.

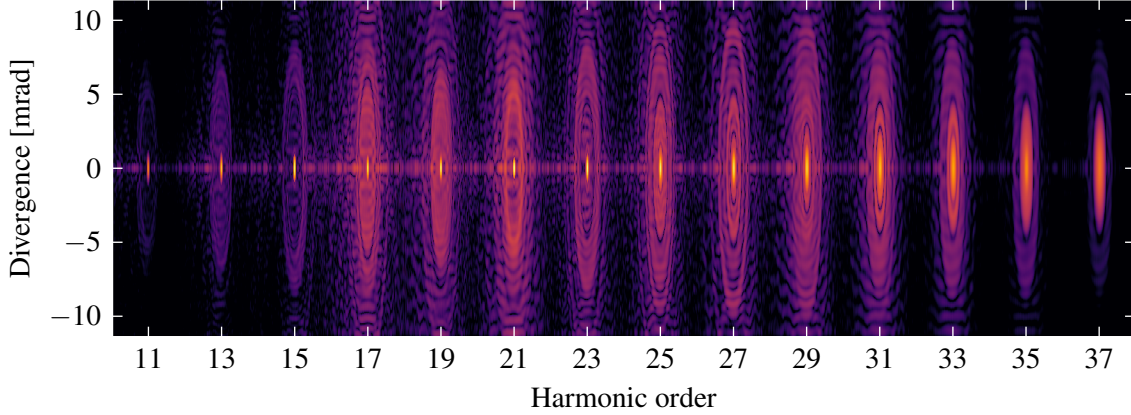


**Figure 9.** Theoretical far-field spectrum [cf. figure 2(a)], for the case for FT-limited driving pulse (170 fs). The single-atom response of a set of atoms is calculated using the TDSE and propagated via a Hankel transform to the far-field.

from different harmonic orders  $q$  and different trajectories  $j$ , we get

$$E(r, t) = \sum_{qj} A_q(r, t) \exp[i\Phi_{qj}(r, t)], \quad (12)$$

with

$$\Phi_{qj} = \Phi_{qj}^0 + \underbrace{\frac{\partial \Phi_{qj}}{\partial I}}_{\alpha_{qj}} I(r, t) + \mathcal{O}\left(\frac{\partial^2 \Phi_{qj}}{\partial I^2}\right),$$

and

$$\Phi_{qj}^0 = q\Phi_0(t) + \Phi_{qj}(I_0)$$

contains the phase of the fundamental  $\Phi_0(t)$  and the atomic dipole response at the peak of the field. In the Gaussian model, the amplitude  $A_q(r, t)$  is of the form  $I^{\frac{n}{2}}(r, t)$ , where the fundamental field intensity is given by

$$\begin{aligned} I(r, t) &= I_0(\tau) \exp\left(-\frac{t^2}{2\tau^2}\right) \exp\left(-\frac{r^2}{2r_0^2}\right) \\ &= I_0(\tau) \exp\left(-\frac{t^2}{2\tau^2}\right) \left[1 - \frac{r^2}{2r_0^2} + \frac{r^4}{8r_0^4} + \mathcal{O}(r^6)\right]. \end{aligned} \quad (13)$$

The normal approximation is to neglect terms of  $\mathcal{O}\left(\frac{\partial^2 \Phi_{qj}}{\partial I^2}\right)$  and higher. Furthermore, it is only possible to analytically propagate the emission to the far-field if the radial profile of the intensity in the phase is approximated up to second order in  $r$ . By including higher-order terms of the spatial profile through a numerical far-field transform, ring structures appear in the far-field amplitude (see figure 10). It is not enough, however, to fully explain the off-axis behaviour of the interference rings – the long trajectory also probes a wider range of intensities, also those for which a certain harmonic would be



considered to be in the cut-off regime. This means we cannot ignore the influence of  $\frac{\partial^2 \Phi_{qj}}{\partial I^2}$  and higher-order terms in the expansion of the phase with respect to the intensity. The effects of these considerations will be briefly surveyed below.

### 6.1. Adiabatic model

The Gaussian model in its simplest form does not explain the correct behaviour of the off-axis emission. To find the missing link, we employ an adiabatic model, where instead of assuming the form (12), we opt for something in-between (11) and (12):

$$A(r) = \sum_q a[q; I(r)], \quad (14)$$

that is, we still decompose the emission into different harmonic orders, but it is not trajectory-resolved anymore.  $a[q; I(r)]$  can be the dipole acceleration moment for harmonic order  $q$  as calculated using the TDSE, in the manner described in section 5, or the dipole spectrum from the SFA. The model is adiabatic inasmuch it does not consider the temporal intensity variation of the driving pulse, but only the spatial intensity variation  $I(r)$  at the peak of the pulse. Furthermore, only emission from the focal plane is considered.

### 6.2. Exact far-field propagation

The far-field amplitude of the emission is found by propagation. In cylindrical coordinates and cylindrical symmetry, this is given by [36]:

$$U_0(\rho) = -i \frac{k}{2\pi z} \exp(ikz) \exp\left(i \frac{k}{2z} \rho^2\right) \mathcal{H}_0\{A(r)\}(k\rho/2\pi z), \quad (15)$$

where  $\mathcal{H}_0\{A(r)\}$  is the zeroth-order Hankel transform of the near-field radial amplitude  $A(r)$ ,  $r$  is the near-field radial coordinate,  $\rho$  is the far-field radial coordinate,  $k$  is the wavevector  $q2\pi/\lambda$  ( $q$  is the harmonic order and  $\lambda$  is the fundamental wavelength) and  $z$  is the propagation distance. The Hankel transform is computed numerically using the algorithm presented in [37].

### 6.3. Off-axis interference structures

Propagating a Gaussian profile with a non-flat phase variation gives modulation of the far-field amplitude, as seen in figure 10. Depending on the form of the near-field phase variation with the spatial profile, different structures appear.

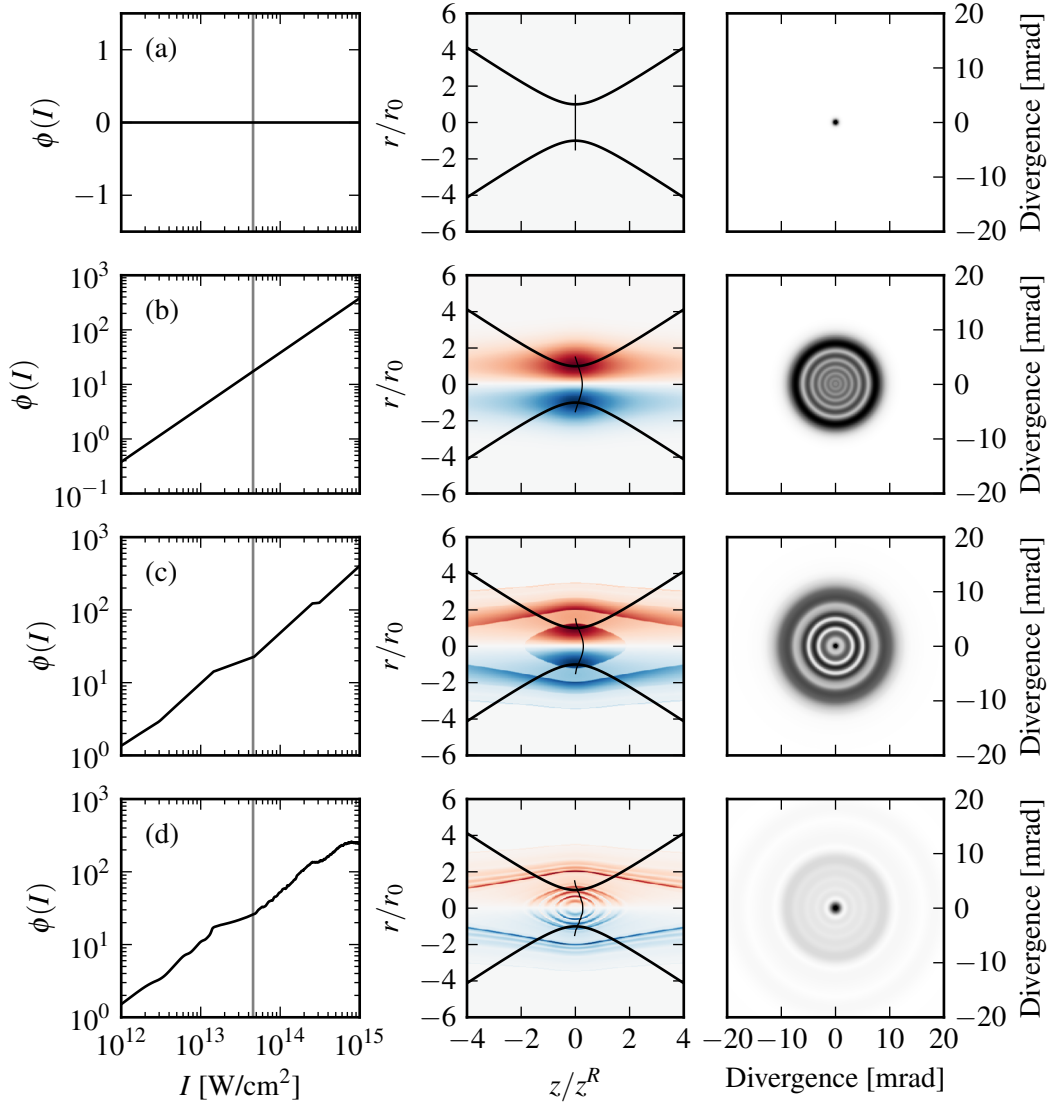


**Figure 10.** Explanation of how the off-axis rings come about. The left-most column shows the phase variation of HH25 in the focal plane, as a function of the fundamental intensity, for the case of no variation (a), a phase proportional to the intensity (b), a crude fit to the phase as calculated by the SFA (c) and the full SFA phase (d). The second case corresponds to (4). The grey, vertical line indicates the cut-off intensity for HH25; for lower intensities, HH25 is a cut-off harmonic, while for higher intensities, it is in the plateau regime. The middle column indicates with solid black lines, the beam waist of the driving field as a function of  $z$ , and the wavefront in the focal plane. The colour map behind shows  $\frac{\partial \phi}{\partial r}$ , which is related to the  $k$  vector; emission from areas of the same colour will have the same direction. The right-most column shows the far-field amplitude. With a flat phase in the focal plane, the Gaussian shape will be preserved. With a simple Gaussian phase (as the intensity profile of the fundamental is Gaussian) in the near-field, ring structures will appear in the far-field amplitude. With more complicated phase behaviour in the near-field, the far-field amplitude will also be more complicated.

In figure 11, the interference pattern for  $q = 25$  is displayed, from the experiment as well as calculated using the adiabatic model, for a few different phase variations with the spatial profile. Whereas both the TDSE and the SFA qualitatively agree quite well with the experiment, the Gaussian beam model does not. It is thus necessary, but not sufficient, to include higher-order terms in the expansion of the intensity profile. Indeed, one must also include higher-order terms in the variation of the phase with the intensity. For the short–long interference, this mainly takes place where two trajectories actually *exist*, namely in the plateau regime. The values of  $\alpha_{s/l}$  as presented in tables 1, 2, reflect this by successfully reproducing the short–long interference, but not the long–long, as is evident when comparing with the TDSE/SFA.

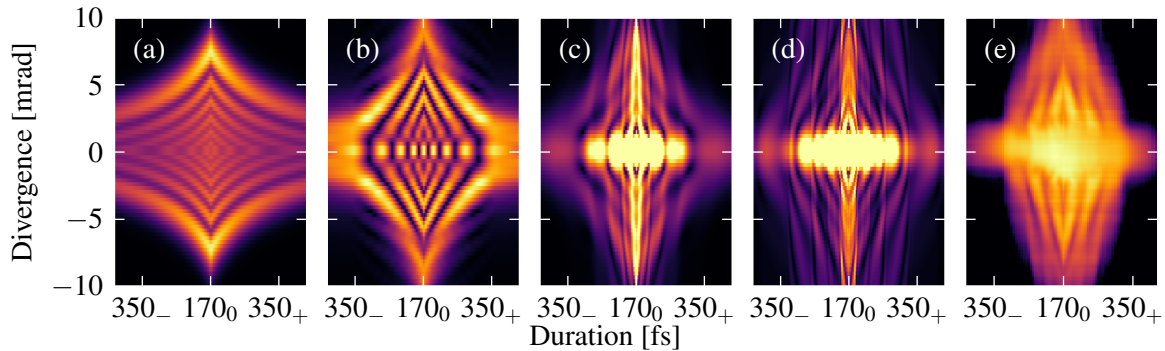


**Figure 11.** Far-field propagation of HH25 for a few different cases: (a) Gaussian model, long trajectory only [figure 10 (b)], (b) SFA log-fit phase [figure 10 (c)], (c) SFA [figure 10 (d)], (d) TDSE, (e) experiment. The short–long trajectory contributions has been saturated to focus on the off-axis interference; the colour scale of the theory (a–d) is linear while that of the experiment (e) is logarithmic as above, due to the much higher dynamic range of the theory.

It cannot be said that the model presented in figure 10 (c), figure 11 (b) only probes the long–long interference, since it is a fit to the phase as given by the SFA; however, as seen in figure 8, the SFA underestimates the short trajectory contribution compared the long trajectory. A crude fit to the SFA phase would thus smooth out any contribution of low amplitude such as the short trajectory one. We can thus say that the model essentially shows the long trajectory behaviour as is apparent from the emphasis on off-axis ring behaviour and suppression of the short–long interference at 0 mrad, which *is* visible in the SFA calculation shown in figure 11 (c).

## 7. Discussion

We find that our mathematical models agree well with the experimental data in the central regions of the spatial and spectral lineouts (figures 5 and 6). They show the robustness of the simple model introduced in [14], even when it is extended to chirped driving fields. It is a clear sign of QPI, similar to the one described in [38], where QPI was studied using excitation by a weak perturbation consisting of a laser pulse with

controlled delay. In analogy with that study, we can think of varying the chirp of the driving pulse as the addition of a controlled perturbation to the driving field.

As noted above, the pulse intensity is only dependent on the magnitude of the chirp parameter  $b$ . This behaviour is clearly reflected in the spatial lineouts, for which the peak intensity is the parameter with largest influence; the lineouts are vertically and horizontally symmetric. The data presented in figure 5(a) are analogue to the intensity scans presented in earlier work [17, 39, 40, 41, 42, 19]. However, the sign of the chirp parameter is important in the spectral lineouts, which substantially differ for negatively and positively chirped driving laser pulses.

The values found by comparison of our mathematical model with the experimental data are in good agreement with the theoretical prediction for  $\alpha_l$  in the whole region of  $q$  and for  $\alpha_s$  close to the cut-off region (see figure 7). Our measured and calculated values of  $\alpha_l$  are also in good agreement with earlier experimental work [15, 19] and theoretical predictions [24, 25, 43, 40]. In this study we have consistently extracted, in both the spectral and spatial measurements, negative values for  $\alpha_s$  for a range of harmonics below and near the ionization threshold. While negative values of  $\alpha_s$  have been theoretically predicted [24, 25], this is to our knowledge the first experimental measurement of negative  $\alpha_s$ . Also our theoretical data as calculated by the TDSE yield negative values of  $\alpha_s$  for the low orders, although not in perfect agreement with the experimental data. It is worth noting that negative values of  $\alpha_s$  are a clear sign of interactions between the returning electron wave packet and the ionic core, i.e. that the atomic potential cannot be neglected in the description of the low-order short-trajectory harmonics. If this effect can be reproduced with even higher precision, it could lead to either a possible improvement of the accuracy of the short-range part of the pseudo-potential used or point towards the need for inclusion of multi-electron effects in the description of the atom used in the calculations.

We have shown in this paper that it is possible to measure  $\alpha_{s/l}$  for the different harmonics. To fully characterize the temporal structure of the generated radiation, however, it is not enough to determine the values of  $\alpha_{s/l}$  for the different frequency components. One would also need to measure the value of  $\Phi_{s/l}^0$  in (4). Using our method, we would also be able to determine  $|\Phi_s^0 - \Phi_l^0|$  to within  $2\pi$ , but not their absolute values, therefore prohibiting the full temporal reconstruction. If one would have interference between, e.g., the long trajectories of two neighbouring harmonics as was the case in [22], one would be able to determine  $\Phi_l^0(q) - \Phi_l^0(q+1)$ , thereby enabling the full reconstruction.

Under our experimental conditions, the harmonics  $q = 11$  and  $q = 13$  correspond to energies below the ionization potential threshold  $I_p$  and are so called below-threshold harmonics. In both cases, we observed the QPI mainly in the divergence lineouts. The experimental observation and theoretical explanation of the QPI for below-threshold harmonics were first made by D. C. Yost et al. in 2009 [31] and  $\alpha_l^*$  was expected to be  $\alpha_l^* \approx 2.5\pi - 3\pi$  and  $\alpha_s^* \approx 0$ . However, in our model we found values  $\alpha_l^* \approx 2\pi$  and  $\alpha_s^* \approx -0.4\pi$ ; these values are in a good agreement with later theoretical calculations

[43, 26].

The prominent ring structures, clearly observed for regions of large spatial and spectral divergence, thus mainly due to the long trajectory, are covered by our extended model. The rings appear when higher orders than parabolic in the phase curvature are included in the propagation of the Gaussian beams. To reproduce the detailed structures of the rings, one has to also include higher orders in the intensity dependence of the phase. This is of particular importance for harmonics that have comparable contributions from the plateau and cut-off regimes. In [20], similar structures were observed, interpreted as temporal Maker fringes, e.g. an effect of phase matching between subsequent planes of generation. The presence of this kind of phase matching in the present work cannot be ruled out, but the qualitative agreement of our theoretical results [figure 11(c–d)] with the experimental results [figure 11(e)] suggests that the explanation presented here is viable.

## 8. Summary

In this paper, we have presented experimental data with interference structures, observed in HHG from argon. The structures are of two kinds; firstly due to QPI between the first two trajectories and secondly due to long trajectory emission from atoms experiencing different local field strengths. The former interference has been systematically investigated by varying the chirp of the driving laser pulses and the observed patterns are well explained by a simple mathematical model based on a semi-classical description of HHG. By careful comparison of the experimental observations with the model, we are able to determine the dipole phase parameters  $\alpha_s$  and  $\alpha_l$  for  $q = 11 - 37$ , which are in a good agreement with theoretical predictions ([25]), except for the short trajectory contribution in the below-threshold harmonics and plateau regions, where we found  $\alpha_s^*$  to be negative with a value  $\alpha_s^* \approx -0.4\pi$ .

Furthermore, the long trajectory interference was successfully modelled by taking into account phase curvature effects beyond the parabolic term. It was shown that the variation of the dipole phase parameters with respect to intensity has to be considered, to obtain the right behaviour of the resultant interference patterns.

## Acknowledgments

This research was supported by the Swedish Foundation for Strategic Research, the Swedish Research Council and the Knut and Alice Wallenberg Foundation and by funding from the NSF under grant PHY-1307083 and PHY-1403236. The quantum mechanical calculations were performed at the Lunarc computing facility at Lund University, within the supercomputing network of Sweden, SNIC, under the project SNIC 2015/1-386.

## Appendix A. Derivation of Gaussian model

### Appendix A.1. Divergence model

Modelling the spatial profiles, we suppose that the main contribution to the generated HHs arises around the temporal maximum of the laser peak  $I_0(\tau)$ , that the driving laser field has a Gaussian profile in the focal plane ( $z = 0$ ) characterized by the beam waist  $r_0$ , and that the generated HH fields of the long and short trajectory ( $E_s^q, E_l^q$ ) can be expressed [using (4)] as

$$\begin{aligned} E_{s/l}^q &= C_{s/l} \left[ \sqrt{I_0(\tau)} \exp\left(-\frac{r^2}{r_0^2}\right) \right]^n e^{i\Phi_{s/l}} \\ &= C_{s/l} \left[ \sqrt{I_0(\tau)} \exp\left(-\frac{r^2}{r_0^2}\right) \right]^n e^{i\Phi_{s/l}^0} \exp\left[ i\alpha_{s/l} I_0(\tau) \exp\left(-\frac{2r^2}{r_0^2}\right) \right], \end{aligned} \quad (\text{A.1})$$

where  $C_{s/l}$  is a proportionality constant and  $n$  is the nonlinearity order of the HH conversion. By Taylor expansion to second order in  $r$ , the phase term  $i\alpha_{s/l} I_0(\tau) \exp\left(-\frac{2r^2}{r_0^2}\right)$  can be simplified to  $i\alpha_{s/l} I_0(\tau) - i2\alpha_{s/l} I_0(\tau) \frac{r^2}{r_0^2}$ . In this approximation the generated field has a Gaussian intensity profile, a parabolic wavefront, and a phase offset. It is straightforward to identify these with a wavefront and an intensity profile of a *shifted* Gaussian beam (GB), which has its waist position located at  $-z_{s/l}^f$ :

$$E_{s/l}(r, z = 0) = E_{0s/l} \frac{w_{0s/l}}{w(z_{s/l}^f)} \exp\left[ -\frac{r^2}{w^2(z_{s/l}^f)} - ik_q z_{s/l}^f - ik_q \frac{r^2}{2R_{s/l}(z_{s/l}^f)} + i\zeta(z_{s/l}^f) + i\eta_{s/l} \right]. \quad (\text{A.2})$$

Subsequently the propagation of the generated HH can be treated as a propagation of two GBs. These sought-after GBs can be fully characterized by the amplitudes  $E_{0s/l}$ , the distances of their waists from the HH interaction region (plane)  $z_{s/l}^f$ , the Rayleigh distances  $z_{s/l}^R$ , the wavevector of the generated HH  $k_q$  (corresponding to the wavelength  $\lambda_q$ ), and the phases  $\eta_{s/l}$ .  $\zeta(z) = \arctan(z/z^R)$  is the Gouy phase. For a thorough treatment of GBs, we refer the reader to [44].  $k_q$  is given and all other variables can be found by comparing (A.1) in the parabolic approximation and (A.2). From comparison of the spatial parts of the equations, we get

$$E_{0s/l} = C_{s/l} \frac{w(z_{s/l}^f)}{w_{0s/l}} I_0^{\frac{n}{2}}(\tau), \quad w(z_{s/l}^f) = \frac{r_0}{\sqrt{n}}, \quad (\text{A.3})$$

and from the phase parts we find

$$R_{s/l}^f = R(z_{s/l}^f) = \frac{kr_0^2}{4\alpha_{s/l} I_0(\tau)}, \quad \eta_{s/l} = \Phi_{s/l}^0 + \alpha_{s/l} I_0(\tau) + k_q z_{s/l}^f - \zeta(z_{s/l}^f). \quad (\text{A.4})$$

If we express the (A.3) and (A.4) using GBs

$$w_{s/l}(z) = w_{0s/l} \left[ 1 + z^2 / (z_{s/l}^R)^2 \right]^{1/2}, \quad R_{s/l}(z) = z \left[ 1 + (z_{s/l}^R)^2 / z^2 \right],$$

we get a set of two equations for two unknown variables  $z_{s/l}^f$  and  $z_{s/l}^R$  with solutions

$$z_{s/l}^R = \frac{\pi\lambda_q(R_{s/l}^f)^2 r_0^2/n}{\lambda_q^2(R_{s/l}^f)^2 + \pi r_0^4/n^2}, \quad z_{s/l}^f = \frac{\pi^2 R_{s/l}^f r_0^4/n^2}{\lambda_q^2(R_{s/l}^f)^2 + \pi r_0^4/n^2}. \quad (\text{A.5})$$

Finally, the generated HH field at the detector at distance  $z$  can be modelled as a sum of GBs representing short and long QP contribution,  $E_{\text{detector}}(r, z) = E_s(r, z) + E_l(r, z)$ , where

$$E_{s/l}(r, z) = E_{0s/l} \frac{w_{0s/l}}{w_{s/l}(\tilde{z}_{s/l})} \exp \left[ -\frac{r^2}{w_{s/l}^2(\tilde{z}_{s/l})} - ik_q \tilde{z}_{s/l} - ik_q \frac{r^2}{2R_{s/l}(\tilde{z}_{s/l})} + i\zeta(\tilde{z}_{s/l}) + i\eta_{s/l} \right], \quad (\text{A.6})$$

and  $\tilde{z}_{s/l} \equiv z + z_{s/l}^f$ . The quantity that is measured is proportional to

$$|E_{\text{detector}}(r, z)|^2 = |E_s(r, z)|^2 + |E_l(r, z)|^2 + 2|E_s(r, z)||E_l(r, z)| \cos[\chi(r, z)], \quad (\text{A.7})$$

where

$$\begin{aligned} \chi(r, z) = & -\frac{k_q r^2}{2} \left[ \frac{1}{R_s(\tilde{z}_s)} - \frac{1}{R_l(\tilde{z}_l)} \right] + [\zeta(\tilde{z}_s) - \zeta(\tilde{z}_l)] - [\zeta(z_s^f) - \zeta(z_l^f)] \\ & + (\Phi_s^0 - \Phi_l^0) + (\alpha_s - \alpha_l) I_0(\tau). \end{aligned} \quad (\text{A.8})$$

### Appendix A.2. Spectral model

Turning to the spectral behaviour of the harmonics, we can assume that the main contribution is generated in the middle of the focus and that we can neglect the spatial variation of  $\Phi_{s/l}$ . We describe the short and long trajectory contributions as

$$E_{s/l}(t) = E_{0s/l}(t) \exp [i q \omega(t) t + i \Phi_{s/l}(t)], \quad (\text{A.9})$$

where  $E_{0s/l}(t)$  is the amplitude of the generated field approximated by

$$E_{0s/l}(t) = C_{s/l} I^{\frac{n}{2}}(t). \quad (\text{A.10})$$

$I(t)$  is the time-varying intensity in the middle of generation plane and  $\omega(t)$  is the frequency of the driving laser. The instantaneous frequency of the generated HH  $\omega_{s/l}(t)$  is determined as the time derivative of the phase of (A.9):

$$\omega_{s/l}(t) = q\omega(t) + \alpha_{s/l} \frac{\partial I(t)}{\partial t}. \quad (\text{A.11})$$

We suppose that the driving pulse is linearly chirped

$$\omega(t) = \omega_0 + b(\tau)t, \quad (\text{A.12})$$

where  $\omega_0$  is the central frequency of the driving laser field and  $b(\tau)$  is the chirp rate. The driving field intensity varies as

$$I(t) = I_0(\tau) \exp \left( -\frac{4 \ln 2}{\tau^2} t^2 \right), \quad (\text{A.13})$$

where  $I_0(\tau)$  can be determined from (2). The chirp rate  $b$  is then related to the duration of the laser pulse  $\tau$  and to the duration of the Fourier transform limited pulse  $\tau_{\text{FT}}$  as

$$b(\tau) = \pm \frac{4 \ln 2}{\tau^2} \sqrt{\frac{\tau^2}{\tau_{\text{FT}}^2} - 1}. \quad (\text{A.14})$$

In the presented lineouts, the negatively chirped pulses are on the left side (negative sign in the above equation), whereas the positively chirped pulses (positive sign) on the right side.

Together with (A.12) and the time derivative of (A.13), we find the instantaneous frequency of the generated HH:

$$\omega_{s/l}(t) = q\omega_0 + qb(\tau)t - \alpha_{s/l} \frac{8 \ln 2}{\tau^2} I(t). \quad (\text{A.15})$$

For our simulation, the generated HH field is described as

$$E_{s/l}(t) = C_{s/l} I^{\frac{n}{2}}(t) \exp \left[ iq\omega_0 t + i \frac{qb(\tau)}{2} t^2 + i\alpha_{s/l} I(t) + i\Phi_{s/l}^0 \right]. \quad (\text{A.16})$$

The far-field spectra of the generated HHs are computed as the Fourier transform of the sum of the fields generated by the short and long trajectory contributions

$$S(\omega) = \mathcal{F}[E_s(t) + E_l(t)], \quad (\text{A.17})$$

and the intensity in the far field is given by

$$I(\omega) \propto |S(\omega)|^2. \quad (\text{A.18})$$



## References

- [1] McPherson A, Gibson G, Jara H, Johann U, Luk T S, McIntyre I A, Boyer K and Rhodes C K 1987 *J. Opt. Soc. Am. B* **4** 595 ISSN 1520-8540 URL <http://dx.doi.org/10.1364/JOSAB.4.000595>
- [2] Ferray M, L'Huillier A, Li X F, Lompre L A, Mainfray G and Manus C 1988 *Journal of Physics B: Atomic, Molecular and Optical Physics* **21** L31–L35 ISSN 1361-6455 URL <http://dx.doi.org/10.1088/0953-4075/21/3/001>
- [3] Corkum P B and Krausz F 2007 *Nature Physics* **3** 381–387 URL <http://dx.doi.org/10.1038/nphys620>
- [4] Drescher M, Hentschel M, Kienberger R, Uiberacker M, Yakovlev V, Scrinzi A, Westerwalbesloh T, Kleineberg U, Heinzmann U and Krausz F 2002 *Nature* **419** 803–807 URL <http://dx.doi.org/10.1038/nature01143>
- [5] Mauritsson J, Remetter T, Swoboda M, Klünder K, L'Huillier A, Schafer K J, Ghafur O, Kelkensberg F, Siu W, Johnsson P, Vrakking M J J, Znakovskaya I, Uphues T, Zharebtsov S, Kling M F, Lépine F, Benedetti E, Ferrari F, Sansone G and Nisoli M 2010 *Physical Review Letters* **105**(5) 053001
- [6] Schultze M, Fieß M, Karpowicz N, Gagnon J, Korbman M, Hofstetter M, Neppl S, Cavalieri A, Komninos Y, Mercuris T *et al.* 2010 *Science* **328** 1658–1662 URL <http://www.sciencemag.org/content/328/5986/1658.short>
- [7] Klünder K, Dahlström J M, Gisselbrecht M, Fordell T, Swoboda M, Guénot D, Johnsson P, Caillat J, Mauritsson J, Maquet A and *et al* 2011 *Physical Review Letters* **106** ISSN 1079-7114 URL <http://dx.doi.org/10.1103/PhysRevLett.106.143002>
- [8] Schafer K J, Yang B, DiMauro L F and Kulander K C 1993 *Physical Review Letters* **70** 1599–1602 ISSN 0031-9007 URL <http://dx.doi.org/10.1103/PhysRevLett.70.1599>
- [9] Corkum P B 1993 *Physical Review Letters* **71** 1994–1997 ISSN 0031-9007 URL <http://dx.doi.org/10.1103/PhysRevLett.71.1994>
- [10] Krause J L, Schafer K J and Kulander K C 1992 *Phys. Rev. Lett.* **68** 3535–3538 URL <http://dx.doi.org/10.1103/PhysRevLett.68.3535>
- [11] Lewenstein M, Balcou P, Ivanov M Y, L'Huillier A and Corkum P B 1994 *Physical Review A* **49** 2117–2132 ISSN 1094-1622 URL <http://dx.doi.org/10.1103/PhysRevA.49.2117>
- [12] Bellini M, Lyngå C, Tozzi A, Gaarde M B, Hänsch T W, L'Huillier A and Wahlström C G 1998 *Physical Review Letters* **81** 297–300 URL <http://dx.doi.org/10.1103/PhysRevLett.81.297>
- [13] Lyngå C, Gaarde M B, Delfin C, Bellini M, Hänsch T W, L'Huillier A and Wahlström C G 1999 *Physical Review A* **60** 4823–4830 ISSN 1094-1622 URL <http://dx.doi.org/10.1103/PhysRevA.60.4823>

- [14] Gaarde M B, Salin F, Constant E, Balcou P, Schafer K J, Kulander K C and L’Huillier A 1999 *Physical Review A* **59** 1367–1373 ISSN 1094-1622 URL <http://dx.doi.org/10.1103/PhysRevA.59.1367>
- [15] Benedetti E, Caumes J P, Sansone G, Stagira S, Vozzi C and Nisoli M 2006 *Optics Express* **14** 2242 ISSN 1094-4087 URL <http://dx.doi.org/10.1364/OE.14.002242>
- [16] Corsi C, Pirri A, Sali E, Tortora A and Bellini M 2006 *Physical Review Letters* **97** ISSN 1079-7114 URL <http://dx.doi.org/10.1103/PhysRevLett.97.023901>
- [17] Zaïr A, Holler M, Guandalini A, Schapper F, Biegert J, Gallmann L, Keller U, Wyatt A S, Monmayrant A, Walmsley I A and et al 2008 *Physical Review Letters* **100** ISSN 1079-7114 URL <http://dx.doi.org/10.1103/PhysRevLett.100.143902>
- [18] Ganeev R A, Hutchison C, Siegel T, Zaïr A and Marangos J P 2011 *Physical Review A* **83** ISSN 1094-1622 URL <http://dx.doi.org/10.1103/PhysRevA.83.063837>
- [19] He L, Lan P, Zhang Q, Zhai C, Wang F, Shi W and Lu P 2015 *Physical Review A* **92** ISSN 1094-1622 URL <http://dx.doi.org/10.1103/PhysRevA.92.043403>
- [20] Heyl C M, GÜdde J, Höfer U and L’Huillier A 2011 *Physical Review Letters* **107** ISSN 1079-7114 URL <http://dx.doi.org/10.1103/PhysRevLett.107.033903>
- [21] Dubrouil A, Hort O, Catoire F, Descamps D, Petit S, Mével E, Strelkov V V and Constant E 2014 *Nature Communications* **5** URL <http://dx.doi.org/10.1038/ncomms5637>
- [22] Sansone G, Benedetti E, Caumes J P, Stagira S, Vozzi C, Pascolini M, Poletto L, Villoresi P, Silvestri S D and Nisoli M 2005 *Phys. Rev. Lett.* **94** URL <http://dx.doi.org/10.1103/PhysRevLett.94.193903>
- [23] Paul P M 2001 *Science* **292** 1689–1692 URL <http://dx.doi.org/10.1126/science.1059413>
- [24] Mauritsson J, Johnsson P, López-Martens R, Varjú K, Kornelis W, Biegert J, Keller U, Gaarde M B, Schafer K J and L’Huillier A 2004 *Physical Review A* **70** ISSN 1094-1622 URL <http://dx.doi.org/10.1103/PhysRevA.70.021801>
- [25] Varjú K, Mairesse Y, Carré B, Gaarde M, Johnsson P, Kazamias S, López-Martens R, Mauritsson J, Schafer K, Balcou P *et al.* 2005 *Journal of Modern Optics* **52** 379–394
- [26] He L, Lan P, Zhai C, Li Y, Wang Z, Zhang Q and Lu P 2015 *Physical Review A* **91** ISSN 1094-1622 URL <http://dx.doi.org/10.1103/PhysRevA.91.023428>
- [27] Salières P, L’Huillier A and Lewenstein M 1995 *Physical Review Letters* **74** 3776–3779 ISSN 1079-7114 URL <http://dx.doi.org/10.1103/PhysRevLett.74.3776>
- [28] Salières P 2001 *Science* **292** 902–905 ISSN 1095-9203

- [29] Lorek E, Larsen E W, Heyl C M, Carlström S, Paleček D, Zigmantas D and Mauritsson J 2014 *Review of Scientific Instruments* **85** 123106 ISSN 1089-7623 URL <http://dx.doi.org/10.1063/1.4902819>
- [30] Murakami M, Mauritsson J and Gaarde M B 2005 *Physical Review A* **72** ISSN 1094-1622 URL <http://dx.doi.org/10.1103/PhysRevA.72.023413>
- [31] Yost D C, Schibli T R, Ye J, Tate J L, Hostetter J, Gaarde M B and Schafer K J 2009 *Nature Physics* **5** 815–820 ISSN 1745-2481 URL <http://dx.doi.org/10.1038/nphys1398>
- [32] Lewenstein M, Salières P and L’Huillier A 1995 *Physical Review A* **52** 4747–4754 ISSN 1094-1622 URL <http://dx.doi.org/10.1103/PhysRevA.52.4747>
- [33] Schafer K J 2009 *Numerical Methods in Strong Field Physics* vol Strong Field Laser Physics (Springer) pp 111–145
- [34] Balcou P, Dederichs A S, Gaarde M B and L’Huillier A 1999 *Journal of Physics B: Atomic, Molecular and Optical Physics* **32** 2973–2989 ISSN 1361-6455 URL <http://dx.doi.org/10.1088/0953-4075/32/12/315>
- [35] Murakami M, Mauritsson J, L’Huillier A, Schafer K J and Gaarde M B 2005 *Physical Review A* **71** ISSN 1094-1622 URL <http://dx.doi.org/10.1103/PhysRevA.71.013410>
- [36] Goodman J 1996 *Introduction to Fourier optics* (New York: McGraw-Hill) ISBN 0071142576
- [37] Guizar-Sicairos M and Gutiérrez-Vega J C 2004 *Journal of the Optical Society of America A* **21** 53 ISSN 1520-8532 URL <http://dx.doi.org/10.1364/JOSAA.21.000053>
- [38] Kim K T, Zhang C, Shiner A D, Kirkwood S E, Frumker E, Gariepy G, Naumov A, Villeneuve D M and Corkum P B 2013 *Nature Physics* **9** 159–163 ISSN 1745-2481 URL <http://dx.doi.org/10.1038/nphys2525>
- [39] Schapper F, Holler M, Auguste T, Zaïr A, Weger M, Salières P, Gallmann L and Keller U 2010 *Optics Express* **18** 2987 ISSN 1094-4087 URL <http://dx.doi.org/10.1364/OE.18.002987>
- [40] Auguste T, Salières P, Wyatt A S, Monmayrant A, Walmsley I A, Cormier E, Zaïr A, Holler M, Guandalini A, Schapper F and et al 2009 *Physical Review A* **80** ISSN 1094-1622 URL <http://dx.doi.org/10.1103/PhysRevA.80.033817>
- [41] Xu H, Xiong H, Zeng Z, Fu Y, Yao J, Li R, Cheng Y and Xu Z 2008 *Physical Review A* **78** ISSN 1094-1622 URL <http://dx.doi.org/10.1103/PhysRevA.78.033841>
- [42] Jiang J, Wei P, Zeng Z, Miao J, Zheng Y, Ge X, Li C, Li R and Xu Z 2014 *Optics Express* **22** 15975 ISSN 1094-4087 URL <http://dx.doi.org/10.1364/OE.22.015975>
- [43] Hostetter J A, Tate J L, Schafer K J and Gaarde M B 2010 *Physical Review A* **82** ISSN 1094-1622 URL <http://dx.doi.org/10.1103/PhysRevA.82.023401>

- [44] Saleh B 2007 *Fundamentals of photonics* (Hoboken, N.J: Wiley-Interscience) ISBN 978-0-471-35832-9